Draft version September 23, 2018
Preprint typeset using LaTeX style emulateapj v. 01/23/15

THE INNER MASS DISTRIBUTION OF THE GRAVITATIONAL LENS SDP.81 FROM ALMA OBSERVATIONS

Kenneth C. Wong[1,*], Sherry H. Suyu[1], and Satoki Matsushita[1]

Draft version September 23, 2018

ABSTRACT

The central image of a strongly lensed background source places constraints on the foreground lens galaxy's inner mass profile slope, core radius and mass of its nuclear supermassive black hole. Using high-resolution long-baseline Atacama Large Millimeter/submillimeter Array (ALMA) observations and archival *Hubble Space Telescope* (*HST*) imaging, we model the gravitational lens H-ATLAS J090311.6+003906 (also known as SDP.81) and search for the demagnified central image. There is central continuum emission from the lens galaxy's active galactic nucleus (AGN) but no evidence of the central lensed image in any molecular line. We use the CO J=5-4 map to determine the flux limit of the central image excluding the AGN continuum. We predict the flux density of the central image and use the limits from the ALMA data to constrain the inner mass distribution of the lens. For the core radius of $0.15''$ measured from *HST* photometry of the lens galaxy assuming that the central flux is completely attributed to the AGN, we find that a black hole mass of $\log(M_{BH}/M_\odot) \gtrsim 8.4$ is preferred. Deeper observations with a detection of the central image will significantly improve the constraints of the inner mass distribution of the lens galaxy.

Subject headings: gravitational lensing: strong

1. INTRODUCTION

Galaxies with bulges harbor supermassive black holes (SMBH) at their centers. The SMBH mass is surprisingly correlated with properties of the bulge (e.g, luminosity, stellar velocity dispersion) despite the bulge extending beyond the black hole's dynamical sphere of influence (e.g., Magorrian et al. 1998; Ferrarese & Merritt 2000; Gebhardt et al. 2000; Gültekin et al. 2009; Kormendy & Ho 2013). Determining the origin of such correlations is important for understanding how galaxies form and evolve. Most direct measurements of black hole masses based on stellar dynamics, gas dynamics or maser dynamics are restricted to galaxies within ~ 150 Mpc (see, e.g., Tables 2 and 3 of Kormendy & Ho 2013, and references therein). Reverberation mapping (Blandford & McKee 1982) can measure black hole masses of active galactic nuclei (AGNs) at distances up to ~ 1 Gpc, especially for the most massive black holes of $\sim 10^9 M_\odot$ (e.g., Peterson 2011). One way to independently measure SMBH masses at these cosmological distances is through strong gravitational lensing.

Strong gravitational lensing occurs when a massive foreground object is located close to the line of sight to a background source. By fitting a mass model to the multiple lensed images of the background source, properties of the mass distribution of the foreground lens galaxy can be inferred. These constraints are strongest within the galaxy's Einstein radius, which is on the scales of a few kpc. Lensing theory predicts that for a non-singular mass distribution, there should be an additional highly-demagnified image very close to the center of the lens. The brightness of this image is highly sensitive to the central mass distribution of the lens on much smaller scales ($\sim$ 100 pc), with more concentrated mass distributions producing greater demagnification. Detection of these central images is extremely challenging due to their low brightness and the fact that they are embedded in emission from the lens galaxy. The best prospects for detection are in radio observations, where lens galaxies generally have very weak emission. Indeed, the only confirmed detection of a central image is of a radio lens (Winn et al. 2004). However, even a non-detection can place constraints on the inner mass distribution (e.g., Zhang et al. 2007).

Recent studies reveal a population of lensed dusty star forming galaxies at $z \sim 2-3$ (e.g., Negrello et al. 2010; Bussmann et al. 2013; Hezaveh et al. 2013; Vieira et al. 2013). Due to the steepness of their luminosity function at the bright end, these galaxies benefit greatly from lensing magnification and are among the brightest sources in wide-area submillimeter surveys (Hezaveh & Holder 2011). Their large submillimeter fluxes make them ideal targets to search for central images. With the high sensitivity and resolution of the Atacama Large Millimeter/submillimeter Array (ALMA), Hezaveh et al. (2015) predict that observations of these lenses could detect their central images and constrain the size of the lens galaxy's core, mass profile slope, and mass of its SMBH.

In this paper, we use the first long-baseline ALMA observations of a strong gravitational lens, H-ATLAS J090311.6+003906 (hereafter SDP.81), to place an upper limit on the flux of the central image and constrain the properties of the innermost regions of the lens galaxy. SDP.81 is a massive elliptical galaxy at $z = 0.2999$ lensing a background dusty star-forming galaxy at $z = 3.042$ into four multiple images (Negrello et al. 2010, 2014). It was identified by Negrello et al. (2010) as one of the brightest sources in the Science Demonstration Phase (SDP) of the *Herschel* Astrophysical Terahertz Large Area Survey (H-ATLAS; Eales et al. 2010).

This paper is organized as follows. In Section 2, we summarize the data used in this analysis. Our lens mod-

[1] Institute of Astronomy and Astrophysics, Academia Sinica (ASIAA), P.O. Box 23-141, Taipei 10617, Taiwan
[*] EACOA Fellow

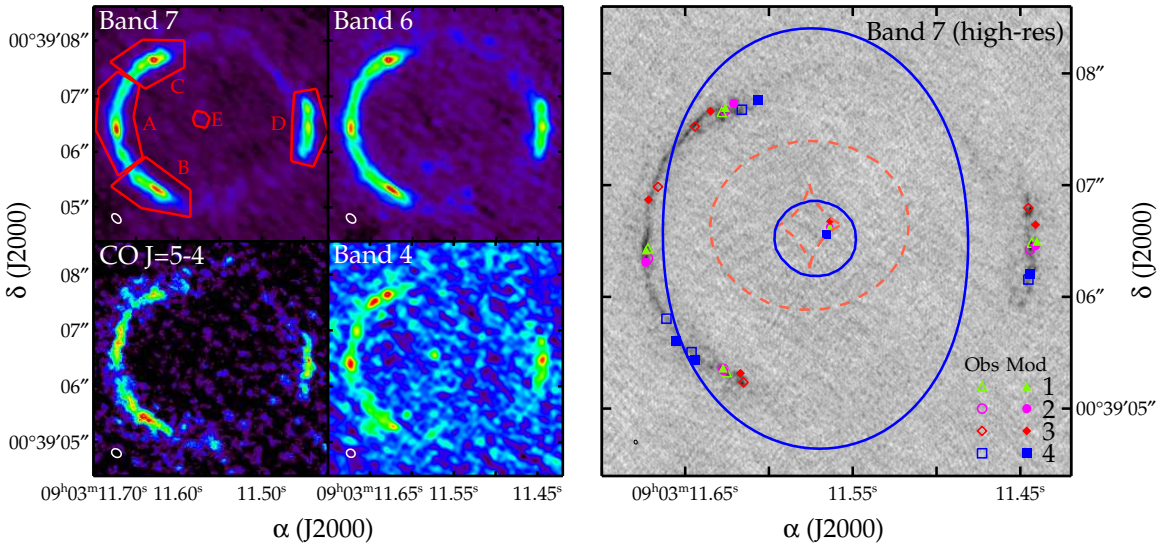

FIG. 1.— **Left:** ALMA images of SDP.81. Shown are the uv-tapered Band 7 continuum (top left), uv-tapered Band 6 continuum (top right), CO J=5-4 (bottom left), and Band 4 continuum (bottom right). The beam size is the white ellipse in the bottom left of each panel. The red regions in the Band 7 continuum image (labeled A–E in order of decreasing flux density) are used to compute the flux densities of the images. **Right:** High-resolution Band 7 continuum negative image. The beam size is the black ellipse in the bottom left. Open symbols are the positions used for the lens modeling for feature 1 (green triangles), 2 (magenta circles), 3 (red diamonds), and 4 (blue squares). Filled symbols are the positions of the corresponding images predicted by our most probable lens model for the $R_{core} = 0.08''$ case (the positions from the $R_{core} = 0.15''$ model are very similar). The small filled symbols near the center are the predicted source positions for the same model. The critical curves (solid blue) and caustics (dashed orange) are overplotted. All images are 4.2″ on a side.

eling procedure is described in Section 3. We present our results in Section 4 and summarize in Section 5. We assume $\Omega_m = 0.3$, $\Omega_\Lambda = 0.7$, and $H_0 = 70\,\mathrm{km\,s^{-1}\,Mpc^{-1}}$. All quantities are given in h_{70} units. At $z = 0.2999$, the angular scale is $1'' = 4.45$ kpc.

2. DATA

2.1. *ALMA Data*

ALMA Science Verification observations of SDP.81 were taken in October 2014 as part of the 2014 ALMA Long Baseline Campaign. Details of the observations are described in ALMA Partnership et al. (2015). We use archival images of the CO J=5-4 line and the Bands 4 (151 GHz) and 6+7 (268 GHz) continuum, CLEANed with the $1000k\lambda uv$ tapering. For the Bands 6 (236 GHz) and 7 (290 GHz) continuum images, we created $1000k\lambda uv$ tapered images from the archival calibrated uv data in the same manner as the other $1000k\lambda uv$ tapered images. The images are shown in Figure 1.

The beam sizes and position angles (measured East of North) are as follows: $0.182'' \times 0.143'', 57.3°$ for CO J=5-4 , $0.158'' \times 0.139'', 61.0°$ for the Band 4 continuum, $0.192'' \times 0.133'', 46.5°$ for the uv-tapered Band 6 continuum, and $0.200'' \times 0.125'', 42.5°$ for the uv-tapered Band 7 continuum. The root mean square (rms) noise level of each map is 0.0166 Jy beam^{-1} km s^{-1} for CO J=5-4 , 0.0115 mJy beam^{-1} for the Band 4 continuum, 0.0200 mJy beam^{-1} for the uv-tapered Band 6 continuum, and 0.0193 mJy beam^{-1} for the uv-tapered Band 7 continuum.

There is compact emission from the center of the system, which was also identified by ALMA Partnership et al. (2015). We distinguish between a central image and emission from the lens galaxy by comparing its SED to that of the primary lensed images (e.g., McKean et al. 2005; More et al. 2008). Its flat SED (see Section 3) indicates that it is not the central image, but rather low-level AGN emission from the lens galaxy (Figure 2). The central image is not detected in any of the continuum-subtracted line emissions, indicating that it is highly demagnified. Being a quad lens, this is expected for SDP.81 since quads generally have more demagnified central images than doubles (Keeton 2003).

2.2. *HST Data*

We use archival *Hubble Space Telescope* (*HST*) Wide Field Camera 3 (WFC3) imaging of SDP.81 to model the light distribution of the lens galaxy and constrain its core radius. The observations were taken in April 2011 (proposal #12194, PI: Negrello). These data were presented in Negrello et al. (2014) and were used to model the lens system (Dye et al. 2014). The observations consist of 712 seconds of exposure time in F110W and 4418 seconds of exposure time in F160W. The data are reduced using DRIZZLEPAC (Gonzaga et al. 2012)[3] with resampling to a 0.065″/pixel scale. The data are shown in the top panels of Figure 3.

3. LENS MODELING

Our lens modeling is performed with GLEE, a software developed by S. H. Suyu and A. Halkola (Suyu & Halkola 2010; Suyu et al. 2012). Lensing mass distributions are parametrized profiles. Model parameters of the lens are constrained through Markov Chain Monte Carlo (MCMC) sampling.

3.1. *Constraints From the Multiple Images*

We visually identify four distinct features in the lensed source from a combination of the high-resolution Band 6

[3] http://drizzlepac.stsci.edu/

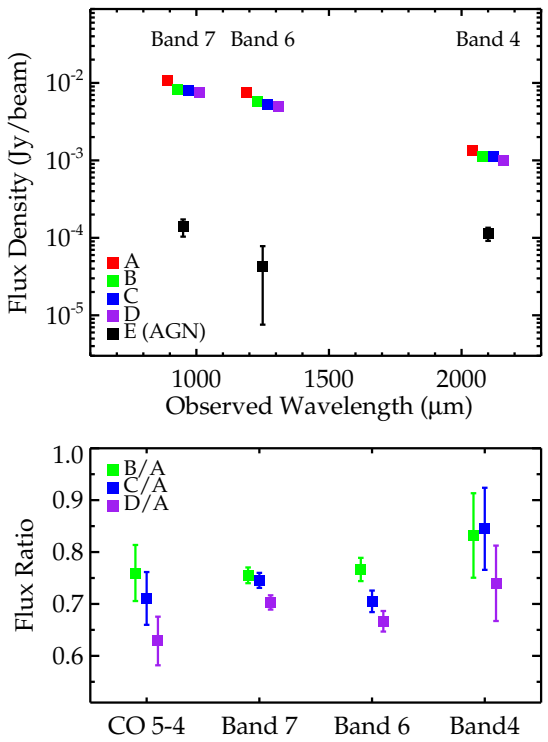

FIG. 2.— **Top:** SED of the four lensed images and central AGN of the lens galaxy. The points are offset in wavelength for clarity. The shape of the AGN SED is distinct from that of the background source, indicating that the emission is from the lens galaxy rather than a central image. **Bottom:** Flux ratios of images B, C, and D relative to image A in the CO J=5-4 and continuum bands.

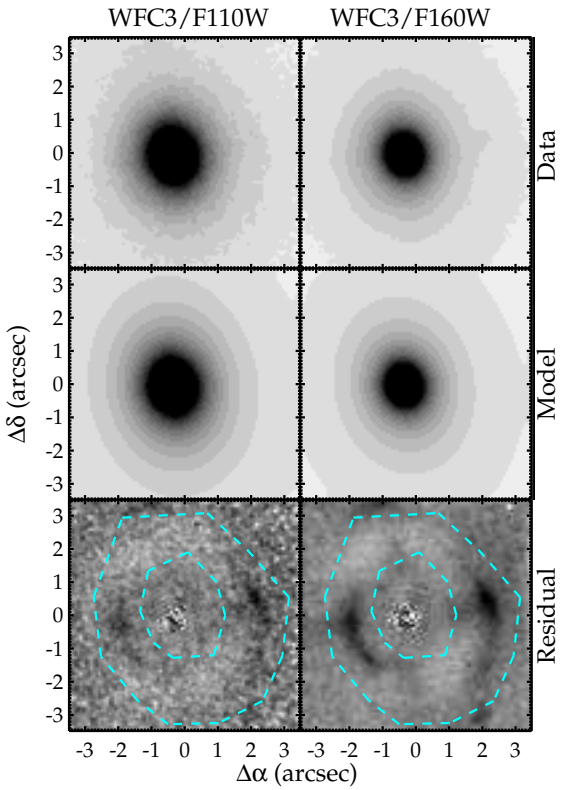

FIG. 3.— **Top:** *HST*/WFC3 imaging of SDP.81 in bands F110W (left) and F160W (right) on a 0.065″/pixel scale. **Middle:** Best-fit models (double power-law plus point source) to the galaxy light distribution. **Bottom:** Residual image when our model is subtracted from the data. The cyan annulus indicates the region that was masked out during the light fitting. The best-fit models give an inner core radius of 0.15″, while the models without a point source give an inner core radius of 0.08″.

and Band 7 continuum, the lower-resolution Band 4 continuum, and combined Band 6+7 continuum data. The locations of the identified features in the CLEANed images are shown as open symbols in Figure 1 (right panel). Features 1 and 2 are identified as two compact star forming clumps in the high-resolution Band 7 continuum image. Features 3 and 4 are identified as broader emission regions in the Band 4 continuum and Band 6+7 continuum images. The positions of 3 and 4 are less precisely identifiable, so their uncertainties are larger as a result.

The flux ratios of individual features are difficult to measure since it is not clear how to define a region that encloses their flux across all wavelengths. We therefore measure fluxes of the entirety of each lensed image (Figure 1, upper left panel) and use those to estimate the flux ratios of the features. We designate the four images A (left arc), B (lower left arc), C (upper left arc), and D (right counterimage). We use the Band 4 continuum, CO J=5-4 , uv-tapered Band 6 continuum, and uv-tapered Band 7 continuum images (Table 1) to estimate flux ratios (Figure 2, bottom panel). Uncertainties on the fluxes in these regions are the background rms multiplied by the square root of the number of beams in the region. The positions and fluxes are given in Table 1.

We use the positions of these features as constraints on the lens model. Since the background source is spatially extended and the magnifications of images A, B and C are high, we do not use the fluxes of these images as constraints due to the high uncertainty from differential magnification (e.g., Hezaveh et al. 2012), which we estimate to be $\sim$ 30-50% from simulations. We use the flux of D and the flux limit of E in the CO J=5-4 image for constraining the inner lens mass distribution.

3.2. *Lens Mass Modeling*

We model the lens as a combination of a cored elliptical power-law mass distribution, a point mass representing the central SMBH, and external shear. The lens model parameters are given in Table 1. We sample the posterior probability distribution of the lens parameters $\boldsymbol{\eta}$ given the observed data $\boldsymbol{d}$:

$$P(\boldsymbol{\eta}|\boldsymbol{d}) \propto L(\boldsymbol{d}|\boldsymbol{\eta})Q(\boldsymbol{\eta}). \quad (1)$$

The likelihood L is

$$L(\boldsymbol{d}|\boldsymbol{\eta}) = L_{\rm pos}(\boldsymbol{d}|\boldsymbol{\eta})L_{\rm flux}(\boldsymbol{d}|\boldsymbol{\eta}), \quad (2)$$

where $L_{\rm pos}$ is associated with the observed image positions A, B, C and D, and $L_{\rm flux}$ is the non-detection of the central image E. Specifically,

$$L_{\rm pos} = \frac{1}{Z_{\rm pos}} \exp\left[-\frac{1}{2}\sum_{j=1}^{N_{\rm f}} \sum_{i=A,B,C,D} \frac{|\boldsymbol{R}_{i,j}^{\rm obs} - \boldsymbol{R}_{i,j}^{\rm pred}(\boldsymbol{\eta})|^2}{\sigma_{i,j}^2}\right] \quad (3)$$

where $N_{\rm f} = 4$ is the number of features/clumps identified in the background source, $\boldsymbol{R}_{i,j}^{\rm obs} = (x_{i,j}^{\rm obs}, y_{i,j}^{\rm obs})$ is the observed image position, $\boldsymbol{R}_{i,j}^{\rm pred}(\boldsymbol{\eta})$ is the predicted/modeled image position, $\sigma_{i,j}$ is the uncertainty

TABLE 1
Image Properties and Model Parameters

Image Position Constraints			
Image ID	α (J2000)[a]	δ (J2000)[a]	Uncertainty ($''$)
A1	09:03:11.673 (-1.515)	+00:39:06.43 (-0.110)	0.03
A2	09:03:11.673 (-1.515)	+00:39:06.34 (-0.200)	0.03
A3	09:03:11.667 (-1.420)	+00:39:06.98 (0.445)	0.12
A4	09:03:11.662 (-1.465)	+00:39:05.80 (-0.735)	0.16
B1	09:03:11.626 (-0.795)	+00:39:05.32 (-1.215)	0.05
B2	09:03:11.628 (-0.830)	+00:39:05.35 (-1.180)	0.05
B3	09:03:11.616 (-0.655)	+00:39:05.23 (-1.305)	0.15
B4	09:03:11.647 (-1.115)	+00:39:05.50 (-1.030)	0.16
C1	09:03:11.629 (-0.850)	+00:39:07.65 (1.115)	0.05
C2	09:03:11.627 (-0.820)	+00:39:07.66 (1.130)	0.05
C3	09:03:11.645 (-1.095)	+00:39:07.52 (0.985)	0.15
C4	09:03:11.617 (-0.675)	+00:39:07.67 (1.140)	0.12
D1	09:03:11.444 (1.920)	+00:39:06.48 (-0.055)	0.05
D2	09:03:11.445 (1.910)	+00:39:06.42 (-0.110)	0.05
D3	09:03:11.446 (1.895)	+00:39:06.79 (0.255)	0.08
D4	09:03:11.446 (1.895)	+00:39:06.15 (-0.380)	0.08

Image Fluxes[b]			
Image	CO J=5-4 (Jy km s^{-1})	Band 4 (mJy)	Band 6 (mJy)	Band 7 (mJy)
A	2.61 ± 0.13	1.33 ± 0.08	7.54 ± 0.14	10.8 ± 0.14
B	2.16 ± 0.12	1.11 ± 0.08	5.78 ± 0.13	8.20 ± 0.13
C	1.81 ± 0.11	1.12 ± 0.07	5.32 ± 0.12	8.09 ± 0.12
D	1.45 ± 0.11	0.99 ± 0.07	5.04 ± 0.12	7.64 ± 0.11
E	0.03 ± 0.03	0.11 ± 0.02	0.04 ± 0.04	0.14 ± 0.04

Lens Model Parameters			
Parameter	Prior[c]	Posterior ($0.08''$ R_{core} prior)	Posterior ($0.15''$ R_{core} prior)
α (J2000)	Gaussian; 09:03:11.572 ($\equiv 0.0$)[a] $\pm 0.005''$	09:03:11.572 (-0.004)[a] $\pm 0.005''$	09:03:11.572 (-0.003)[a] $\pm 0.005''$
δ (J2000)	Gaussian; +00:39:06.54 ($\equiv 0.0$)[a] $\pm 0.005''$	+00:39:06.53 (-0.008)[a] $\pm 0.005''$	+00:39:06.53 (-0.008)[a] $\pm 0.005''$
θ_E ($''$)	Gaussian; 1.56 ± 0.12	1.59 ± 0.02	1.58 ± 0.02
Γ [d]	Gaussian; 0.465 ± 0.03	0.46 ± 0.03	0.46 ± 0.03
b/a	Gaussian; 0.79 ± 0.04	0.82 ± 0.03	0.83 ± 0.03
θ ($^\circ$)[e]	Gaussian; 10.8 ± 6.9	6 ± 5	6 ± 4
R_{core} ($''$)	Gaussian; $(0.08; 0.15) \pm 0.01$	0.08 ± 0.01	0.15 ± 0.01
R_{core} (pc)[f]	Gaussian; $(0.08; 0.15) \pm 0.01$	356 ± 45	668 ± 45
γ_{ext}	Gaussian; 0.04 ± 0.02	0.05 ± 0.01	0.04 ± 0.01
θ_γ ($^\circ$)[e,g]	Uniform; $[-\infty, \infty]$	83 ± 7	82^{+7}_{-8}
$\log(M_{BH})(M_\odot)$	Uniform; [7.5, 9.5]	(see Figure 4)	(see Figure 4)

Predicted Central Image Position		
Parameter	Posterior ($0.08''$ R_{core} prior)	Posterior ($0.15''$ R_{core} prior)
α (J2000)	09:03:11.572 (-0.024)[a] $\pm 0.007''$	09:03:11.576 (-0.007)[a] $^{+0.008''}_{-0.007''}$
δ (J2000)	+00:39:06.53 (-0.040)[a] $\pm 0.005''$	+00:39:06.53 (-0.006)[a] $\pm 0.005''$

Note. — Reported values are medians, with errors corresponding to the 16th and 84th percentiles.
[a]Values in parentheses indicate offset in arcseconds relative to the mass centroid prior.
[b]Fluxes measured from uv-tapered images. Uncertainties calculated as background rms level times square root of the number of beams in region.
[c]Model priors from Dye et al. (2014) based on *HST*/WFC3 data. Core radius prior is from our fits to the WFC3 lens light distribution. For Gaussian priors, the center and width are given. For uniform priors, the range is given.
[d]$\Gamma \equiv (\gamma' - 1)/2$, where the three-dimensional mass density is $\rho(r) = r^{-\gamma'}$.
[e]Angles measured East of North.
[f]Physical R_{core} scale under our assumed cosmology.
[g]$\theta_\gamma = 0^\circ$ corresponds to shearing along North-South direction (i.e. external mass distributions East or West from the lens system).

in the observed image position, and $Z_{\rm pos}$ is the normalization given by

$$Z_{\rm pos} = (2\pi)^{N_{\rm pos}} \prod_{j=1}^{N_{\rm f}} \prod_{i=A,B,C,D} \sigma_{i,j}^2 \quad (4)$$

with $N_{\rm pos} = 16$ as the total number of image positions identified. The non-detection likelihood is

$$L_{\rm flux} = \frac{1}{\sqrt{2\pi}\sigma_{\rm CO}} \exp\left[-\frac{f_{\rm E}^{\rm pred}(\boldsymbol{\eta})^2}{2\sigma_{\rm CO}^2}\right], \quad (5)$$

where $\sigma_{\rm CO}$ is the background rms in the CO J=5-4 image and $f_{\rm E}^{\rm pred}(\boldsymbol{\eta})$ is the predicted flux density of image E that is obtained by multiplying the observed integrated flux density of image D with the modeled magnification ratio μ_E/μ_D. We incorporate uncertainty in the flux density of image D by drawing from a Gaussian distribution set by the measured value of $1.45 \pm 0.11\,{\rm Jy\,km\,s^{-1}}$. We use the CO J=5-4 flux density because there is no contamination from the AGN of the lens galaxy after the continuum subtraction.

The prior $Q(\boldsymbol{\eta})$ in equation (1) on most of the parameters are taken from Dye et al. (2014) based on the *HST*/WFC3 data (see Table 1). We set our prior on $\rm R_{core}$ by fitting light profiles to the WFC3 data, excluding an annular region containing the lensed images (Figure 3). We fit the lens light with a double cored power-law profile and constrain $\rm R_{core}$ to be $0.08 \pm 0.01''$ (≈ 356 pc) in both bands. We also fit a double power-law plus point source (convolved with the point spread function) to account for possible low-level AGN emission, which gives a core radius of $0.15 \pm 0.01''$ (≈ 668 pc). We test both cases as priors on the core of the mass profile, as the compact central flux could be due to either AGN activity or stars. We assume that the SMBH is located at the center of the mass distribution and adopt a uniform prior on its logarithmic mass.

In practice, we first sample $L_{\rm pos} \times Q$ via MCMC of chain length 5×10^5, and then weight these samples by $L_{\rm flux}$.

There is a satellite galaxy $\sim 4.5''$ from the lens center, which is close enough that its influence may not be adequately described by external shear alone (McCully et al. 2014). Its integrated light in F160W is $\sim 1\%$ that of the lens galaxy. We test a model with this galaxy included but our results are unaffected.

4. RESULTS

We present the results of our lens model fitting in Table 1 for models with a core radius prior of $0.08''$ and $0.15''$. Our results are consistent with Rybak et al. (2015)[4], who fit directly to the data in visibility space. Comparing the "Prior" and "Posterior" parameter values, most parameters are better constrained by the multiple image positions identified from the ALMA data. Our models predict the central image to be near the mass center (see Table 1). Since it is not detected, the sampling is relatively insensitive to $\rm R_{core}$, so the posterior of $\rm R_{core}$ is essentially set by the prior determined from the *HST*/WFC3 data. Most model parameters for the two different $\rm R_{core}$ priors are very similar since the different core radii are not affecting the overall fit to images A-D. In the right-hand panel of Figure 1, we show the predicted image positions of the four features in A, B, C and D of the most probable model with the $\rm R_{core} = 0.08''$ prior. For both models, we can reproduce the observed image positions with a reduced $\chi^2 \sim 1$.

The non-detection likelihood in equation (5) places limits on the mass of the SMBH. Figure 4 shows the posterior probability density of the SMBH mass. For $\rm R_{core} = 0.08''$, the lens model is sufficiently cuspy that the predicted central image is substantially demagnified below the flux limit, so the non-detection is unable to add useful information to the SMBH mass. However, for $\rm R_{core} = 0.15''$, the probability density rises sharply at $\log(\rm M_{BH}/M_\odot) \approx 8.4$. This is the mass at which the central image demagnification transitions from being controlled mainly by the mass density of the cored power-law mass distribution to being controlled mainly by the SMBH. The hatched region in Figure 4 shows the 1-σ range of SMBH masses predicted by the $\rm M_{BH}$-$\rm M_{bulge}$ relation of Kormendy & Ho (2013) for SDP.81, assuming the stellar mass determined by Negrello et al. (2014). For $\rm R_{core} = 0.15''$, the non-detection of the central image can tighten the range of likely SMBH masses, albeit marginally. The solid grey region shows the same relation assuming $\rm M_{BH}/M_{bulge} \propto (1+z)^{1.96}$ (Bennert et al. 2011), although the redshift evolution of the $\rm M_{BH}$-$\rm M_{bulge}$ relation is fairly uncertain from current observations.

With deeper observations, tighter constraints can be made if the central image is still undetected. In the lower panels of Figure 4, we show results for a hypothetical observation of SDP.81 with a S/N ratio three times higher than the current CO J=5-4 data. The ALMA observations are starting to be able to constrain the $\rm R_{core} = 0.08''$ model, and the constraints for the $\rm R_{core} = 0.15''$ model much more strongly rule out $\log(\rm M_{BH}/M_\odot) \lesssim 8.4$. The transition SMBH mass for the smaller core radius is lower, $\log(\rm M_{BH}/M_\odot) \approx 8.2$, indicating that a smaller black hole mass is needed to demagnify the central image.

5. CONCLUSIONS

Combining high-resolution long-baseline ALMA data and archival *HST* imaging, we model the gravitational lens SDP.81 and investigate the prospects for detecting the demagnified central image. We detect compact emission region in the central region of the lens, but its SED indicates that it arises from low-level AGN activity in the lens galaxy. There is no evidence for a central image in any molecular lines. Using the positions of four distinct features in the source, we model the mass distribution of the lens galaxy.

Based on the non-detection of the central image in the CO J=5-4 map, we are unable to constrain the SMBH mass for the $\rm R_{core} = 0.08''$ model, but the $\rm R_{core} = 0.15''$ model shows a preference for a SMBH mass of $\log(\rm M_{BH}/M_\odot) \gtrsim 8.4$. Deeper ALMA observations can strengthen this constraint and place limits on the SMBH mass for smaller core radii.

Future ALMA observations of strongly-lensed galaxies, particularly two-image lenses whose central images are

[4] The apparent difference in θ_γ is due to alternate definitions of the shear angle (M. Rybak & S. Vegetti, private communication).

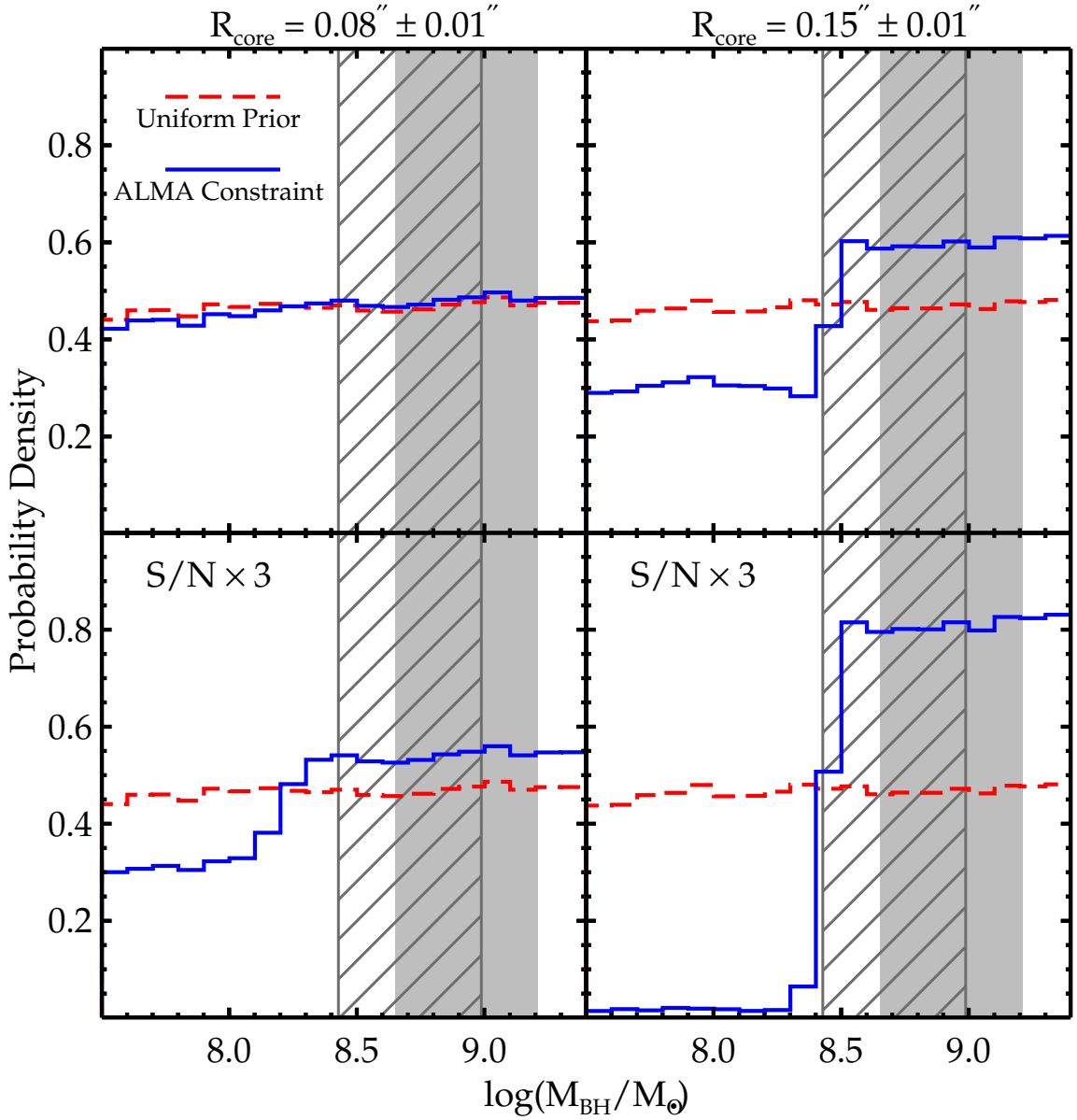

FIG. 4.— Constraints on the SMBH mass from the non-detection of the central image in CO J=5-4 . We show constraints for both the $R_{core} = 0.08''$ (upper left) and $R_{core} = 0.15''$ (upper right) priors. The red line shows the prior probability density, which is uniform in $\log(M_{BH}/M_{\odot})$. The blue line shows the posterior probability density when the non-detection is taken into account. The hatched band shows the 1-σ range of SMBH masses for SDP.81 from the M_{BH}-M_{bulge} relation of Kormendy & Ho (2013), assuming the stellar mass from Negrello et al. (2014), while the solid grey band is the same quantity accounting for redshift evolution of $M_{BH}/M_{bulge} \propto (1+z)^{1.96}$ (Bennert et al. 2011). The non-detection of the central image indicates a preference for $\log(M_{BH}/M_{\odot}) \gtrsim 8.4$ for the $R_{core} = 0.15''$ case, which can marginally improve the constraint from the M_{BH}-M_{bulge} relation alone. The lower panels show the results for a CO J=5-4 observation with a S/N ratio three times higher. With these hypothetical constraints, we can strongly rule out $\log(M_{BH}/M_{\odot}) \lesssim 8.4$ for $R_{core} = 0.15 \pm 0.01''$ and start to see a preference for $\log(M_{BH}/M_{\odot}) \gtrsim 8.2$ when $R_{core} = 0.08 \pm 0.01''$.

less-strongly demagnified, may yield better opportunities for detection. Shorter baseline observations will also be more sensitive and could improve the chance of observing a central image in the molecular lines. Such a detection would place interesting constraints on the central mass distributions of galaxies at cosmological distances and serve as an independent probe of their SMBH mass to better understand the galaxy-black hole connection and its evolution over cosmic time.

We thank Roger Blandford, Nicole Czakon, Aleksi Halkola, Yashar Hezaveh, Luis Ho, Paul Ho, Phil Marshall, John McKean, and Wei-Hao Wang for useful discussions and input. KCW is supported by an EACOA Fellowship awarded by the East Asia Core Observatories Association, which consists of the Academia Sinica Institute of Astronomy and Astrophysics, the National Astronomical Observatory of Japan, the National Astronomical Observatory of China, and the Korea Astronomy and Space Science Institute. This paper makes use of the following ALMA data: ADS/JAO.ALMA#2011.0.00016.SV. ALMA is a partnership of ESO (representing its member states), NSF (USA) and NINS (Japan), together with NRC (Canada)

and NSC and ASIAA (Taiwan), in cooperation with the Republic of Chile. The Joint ALMA Observatory is operated by ESO, AUI/NRAO and NAOJ.

REFERENCES

ALMA Partnership et al. 2015, ApJ, submitted (arXiv:1503.02652)
Bennert, V. N., Auger, M. W., Treu, T., Woo, J.-H., & Malkan, M. A. 2011, ApJ, 742, 107
Blandford, R. D., & McKee, C. F. 1982, ApJ, 255, 419
Bussmann, R. S., et al. 2013, ApJ, 779, 25
Dye, S., et al. 2014, MNRAS, 440, 2013
Eales, S., et al. 2010, PASP, 122, 499
Ferrarese, L., & Merritt, D. 2000, ApJ, 539, L9
Gebhardt, K., et al. 2000, ApJ, 539, L13
Gonzaga, S., Hack, W., Fruchter, A., & Mack, J. 2012, The DrizzlePac Handbook (Baltimore, STScI)
Gültekin, K., et al. 2009, ApJ, 698, 198
Hezaveh, Y. D., & Holder, G. P. 2011, ApJ, 734, 52
Hezaveh, Y. D., Marrone, D. P., & Holder, G. P. 2012, ApJ, 761, 20
Hezaveh, Y. D., Marshall, P. J., & Blandford, R. D. 2015, ApJ, 799, L22
Hezaveh, Y. D., et al. 2013, ApJ, 767, 132
Keeton, C. R. 2003, ApJ, 582, 17
Kormendy, J., & Ho, L. C. 2013, ARA&A, 51, 511
Magorrian, J., et al. 1998, AJ, 115, 2285
McCully, C., Keeton, C. R., Wong, K. C., & Zabludoff, A. I. 2014, MNRAS, 443, 3631
McKean, J. P., et al. 2005, MNRAS, 356, 1009
More, A., McKean, J. P., Muxlow, T. W. B., Porcas, R. W., Fassnacht, C. D., & Koopmans, L. V. E. 2008, MNRAS, 384, 1701
Negrello, M., et al. 2010, Science, 330, 800
—. 2014, MNRAS, 440, 1999
Peterson, B. M. 2011, arXiv:1109.4181
Rybak, M., McKean, J. P., Vegetti, S., Andreani, P., & White, S. D. M. 2015, MNRAS, submitted (arXiv:1503.02025)
Suyu, S. H., & Halkola, A. 2010, A&A, 524, A94
Suyu, S. H., et al. 2012, ApJ, 750, 10
Vieira, J. D., et al. 2013, Nature, 495, 344
Winn, J. N., Rusin, D., & Kochanek, C. S. 2004, Nature, 427, 613
Zhang, M., Jackson, N., Porcas, R. W., & Browne, I. W. A. 2007, MNRAS, 377, 1623